Thermal Annealing Impact on the Sensitivity of Piezomagnetic Surface Acoustic Waveguide to Applied Magnetic Field

Othmane Marbouh, Aurélien Mazzamurro, Olivier Bou Matar, Vincent Maurice, Mohamed Boutghatin, Yannick Dusch, Ahmed Addad, Romain Viard, Philippe Pernod, Rachid Sbiaa, et al.

Thermal annealing impact on the sensitivity of piezomagnetic surface acoustic waveguide to applied magnetic field.

O. Marbouh [1),*], A. Mazzamurro [1)], O. Bou Matar [1)], V. Maurice [1)], M. Boutghatin [1)], Y. Dusch [1)], A. Addad [4)], R. Viard [5)], P. Pernod [1)], R. Sbiaa [3)], A. Tounzi [2)], A. Benabou [2)], N. Tiercelin [1)], A. Talbi [1)].

[1] University of Lille, CNRS, Centrale Lille, University Polytechnique Hauts-de-France, UMR 520 - IEMN, LIA LICS, Lille F-59000, France.

[2] L2EP, University of lille, Bât. ESPRIT - 59655 Villeneuve d'Ascq, France.

[3] Department of Physics, Sultan Qaboos University, P. O. Box 36, PC 123, Muscat, Oman.

[4] University of lille, CNRS, INRA, ENSCL, UMR 8207–UMET– Materials and Transformations Unit, Lille, France.

[5] Group Endress+Hauser, Fribourg-en-Brisgau, Allemagne.

ABSTRACT

Magnetostrictive multilayer thin films, such as $FeCo/TbCo_2$, exhibit significant utility as functionalization materials for Surface Acoustic Wave (SAW) sensors designed for magnetic field measurements. This research investigates the influence of annealing under vacuum and in presence of applied magnetic field at various temperatures over a 4-hour duration on the magnetic properties of the $FeCo/TbCo_2$ thin film and therefore on the sensitivity of shear and Rayleigh acoustic waveguides functionalized with these magnetic layers. The observed effects include a reduction in magnetic anisotropy field (H_A) and an increase in magnetostriction ($b^{\gamma,2}$). X-ray Photoelectron Spectroscopy (XPS) and Transmission Electron Microscopy (TEM) coupled with Energy-Dispersive X-ray Spectroscopy (EDS) microanalysis provide insights into the variations in the properties of the nanostructured magnetic film. To safeguard the magnetic film, a thin layer of SiO_2 is deposited on top, serving as an effective protective shield. The inclusion of this protective layer amplifies sensitivity to applied magnetic fields for modes with shear horizontal polarization, while reducing sensitivity for Rayleigh mode. In ST-cut Quartz, the shear horizontal waves become waveguided upon the incorporation of magnetic thin films, with further enhancement achieved by introducing a SiO2 cap layer. Rayleigh waves are evanescent modes, the penetration depth is in the order of wavelength, and the addition of SiO_2decrease the wave confinement and therefore the sensitivity. The findings of this study are supported by a theoretical model and experimentally validated results.

1. Introduction

Magnetic sensors devices using magnetostrictive thin films are based on the coupling between magnetization and strain. They are typically made of a magnetic material sensitive to magnetic field and a piezoelectric material enabling the transduction of strain.

These piezo-magneto-elastic sensors operate on two primary measurement principles. The first one, called direct magneto-electric effect, relies on AC magnetic fields to induce magnetization oscillations in resonant electromechanical structures [1-4]. The second one, the ΔE effect, uses the dependency of the elastic constants of the magnetic material to the magnetic field in RF electro-acoustic waveguides [5-8].

The incorporation of magnetoelastic thin films into surface acoustic wave (SAW) devices has sparked recent interest. However, the primary focus remains on enhancing the ΔE effect by engineering the acoustic waveguide to leverage confined acoustic waves. This approach aims to increase the ratio of the magnetoelastic thin film thickness to the wavelength, thereby optimizing device performance.

A number of studies carried out by the authors have used a magnetostrictive nanostructured $FeCo/TbCo_2$ as a thin layer for the functionalization of SAW magnetic field sensors [9]. It was shown that the SAW sensor sensitivity relative to the applied magnetic field is mainly dependent on the $FeCo/TbCo_2$ thin films figure of merit (FOM) which is directly proportional to the square of the magnetoelastic coupling $b^{\gamma,2}$ divided by the magnitude of the anisotropy field H_A [8,10] :

$$\mathrm{FOM} = \alpha * \frac{(b^{\gamma,2})^2}{H_A}. \quad (1)$$

Studies carried out in the vicinity of the 2000s on magnetic composite materials such as TbFe/FeCo [11], TbCo/FeCo [12] or TbFeCo/FeCo [13], showed that it is possible to reduce the saturation of the anisotropy field H_A of nanostructured magnetic films and, at the same time, increase their magnetostriction $b^{\gamma,2}$ through thermal annealing by releasing the stresses induced during the deposition of the thin layers.

In this study, we will present the impact of thermal annealing under vacuum $(1 * 10^{-7}\ mbar)$ and bias magnetic field $(50\ mT)$ at different temperatures $(25 - 300°C)$, on the magnetic properties (anisotropy field H_A and magnetostriction coefficient $b^{\gamma,2}$) of the

FeCo/$TbCo_2$ nanostructured thin films and therefore on the sensitivity of the shear and Rayleigh waves to the magnetic field in functionalized SAW sensors. We will also investigate the effect on sensitivity of SiO_2 cap layer deposited on top of the magnetic thin films acting as an effective protective shield against oxidation.

2. Design and Fabrication

As shown on Figure 1, a 2 mm wide and 140 nm thick 17*[$TbCo_2$(4nm)/FeCo(4nm)] uniaxial thin film is deposited by RF-Sputtering under magnetic field ($50\ mT$) and cooling conditions, with a pressure of Ar $1 * 10^{-3}$mbar for $TbCo_2$ and $2 * 10^{-3}$mbar for FeCo , and RF power of 250W and 440 W respectively. The deposition is performed on a ST-cut Quartz substrate between two 50-finger-pair Ti (20nm) / Al (180 nm) Interdigital Transducers (IDT) with 16µm wavelength, and an aperture of 1.8 mm. The deposition was also performed on 25mm^2 Silicon samples and (2mm, 20mm, 50µm) cantilevers for magnetization and magnetostriction measurement respectively. The Shear Horizontal (SH) surface acoustic waves propagate along the Y-axis of ST-cut Quartz, which coincides with the easy axis (EA) of the magnetic film. Similarly, the X-axis corresponds to the hard axis (HA) of the magnetic film, along which the Rayleigh wave propagates. The frequency response of the transmission coefficient S_{21} between the two IDTs measured with a network analyzer (FieldFox N9915B) after deposition of the FeCo/$TbCo_2$ thin film show that the frequencies of the SH and Rayleigh wave are 305 MHz and 195 MHz respectively.

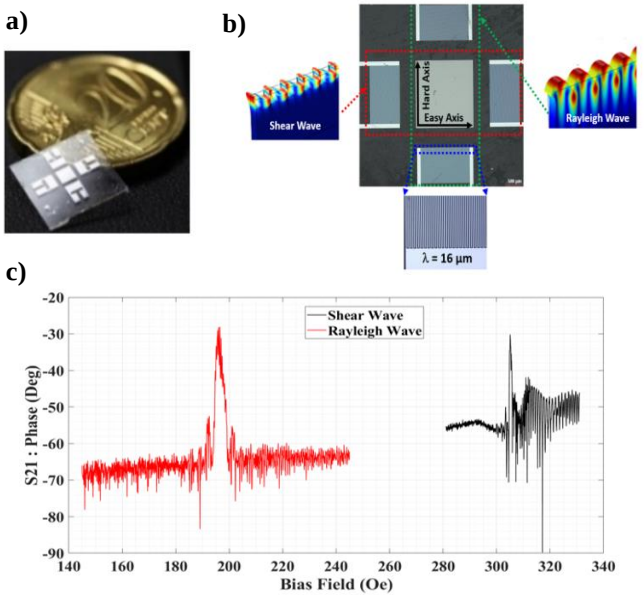

Figure 1 : a) photograph of the fabricated SAW Magnetic sensor. b) Optical image of the SAW device constituted of a uniaxial 140 nm $TbCo_2$/FeCo nanostructured thin film deposited on a ST-cut Quartz substrate. c) View of interdigitated electrodes. d) Responses of surface acoustic wave sensors.

3. Magnetic characterization of $FeCo$ / $TbCo_2$ thin films

The in-plane magnetization of the nanostructured FeCo/$TbCo_2$ thin film has been measured with a Vibrating Sample Magnetometer (VSM) before and after thermal annealing under vacuum ($1 * 10^{-7}\ mbar$) and bias magnetic field ($50\ mT$) at different temperatures, ranging from 25°C to 300°C during 4 hours. The normalized magnetization curves measured on a square Silicon substrate along its Hard (HA) and Easy (EA) Axis are reported on Figure 2.
The magnetization at saturation remain unchanged for the tested annealing temperature, the saturation value of magnetization is close to $2.2 * 10^{-2}\ emu$. Considering the volume of the sample, this value corresponds to 630kA/m. However, the thermal annealing process results in a reduction of the magnetic field anisotropy H_A magnitude from its initial value of $390\ Oe$ at 25°C to $210\ Oe$, as illustrated in Figure 2a). The easy axis becomes more defined as the annealing temperature increases and the coercive force begins to decrease, showing a reduction in the area of the hysteresis loop, see Figure 2b).

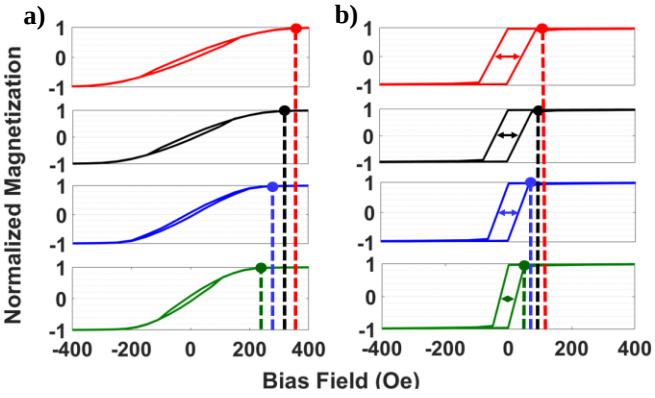

Figure 2 : 17*[$TbCo_2$(4nm)/FeCo(4nm)] thin film magnetization characteristics measured along : a) The hard axis, b) the easy axis, at different temperatures : red without annealing, black annealing at 200 °C, blue annealing at 250 °C and green annealing at 300 °C.

As stated above, the second parameter that contributes to the increase of the FOM of FeCo/$TbCo_2$ thin films is the magnetostriction coefficient $b^{\gamma 2}$, see equation (1). Figure 3 illustrates the variation of magnetostriction, which was measured through deflectometry [14], in a

silicon beam with length, width and thickness of 20mm, 2mm and 50 um respectively. This variation occurs as a magnetic field is applied transversally to the beam, transitioning from positive to negative polarity, using the bench outlined in [15], for nanostructured thin films at various annealing temperature. It is important to note that the maximum of magnetostriction, when the magnetic field is applied longitudinally to the beam when the annealing temperature varies, is negligible (comprised between 0.2 MPa and 0.4 MPa) compared to that field applied transversely. The results demonstrate an enhancement in this characteristic from -5.2 MPa to -7.3 MPa at 300°C.

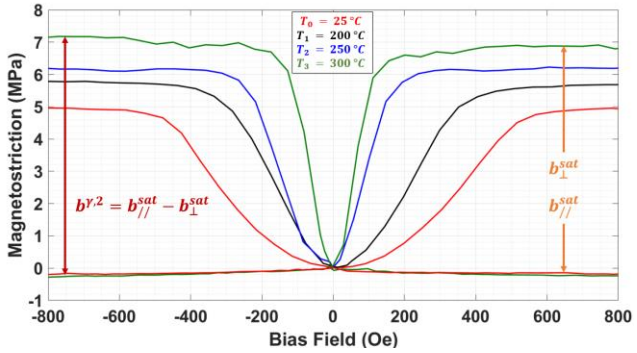

Figure 3 : Magnetostriction measured at different temperatures : red without annealing, black annealing at 200 °C, blue annealing at 250 °C and green annealing at 300 °C.

4. Microanalysis and spectroscopy of $FeCo/TbCo_2$ thin films

To explore the mechanisms behind the decrease in the anisotropy field H_A and the augmentation of the $b^{\gamma,2}$ magnetostriction coefficient due to thermal annealing, two distinct techniques were employed: XPS spectroscopy and TEM imaging combined with EDS microanalysis.

The profile of the distribution of the elements Tb, Fe, Co and O in the FeCo/$TbCo_2$ multilayer stack is obtained by interpreting the XPS spectra using CASAXPS and, more precisely, by integrating them in the energy band under consideration. For the sake of clarity, only the spectra of the $2p^{\frac{3}{2}}$ orbitals of Fe (respectively 4d of Tb) are shown in Figure 4a) (respectively Figure 4b)). The deconvolution of the spectra consists in expressing their different components, each representing an oxidation state, i.e. 0, II, III for Fe and 0, III, IV for Tb. The deconvolution parameters used for the different elements can be found in [16-18] for the energy ranges associated with the different oxidation states of the elements.

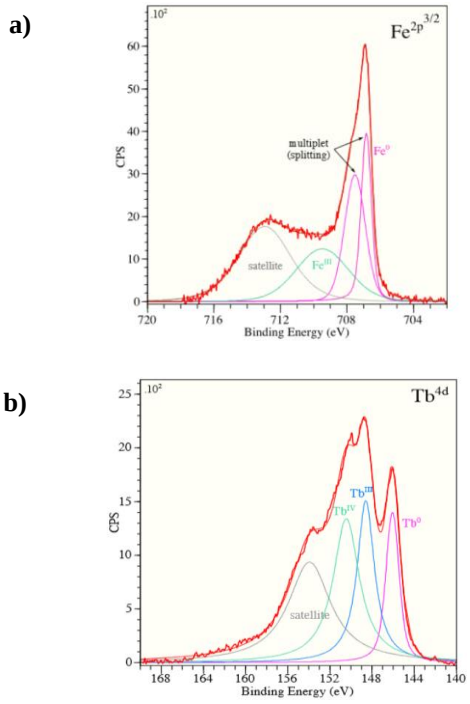

Figure 4 : a) Deconvolution of the XPS spectrum linked to the $\mathbf{2p^{\frac{3}{2}}}$ orbital of Fe highlighting the different oxidation states of Fe. b) Deconvolution of the XPS spectrum linked to the 4d orbital of Tb highlighting the different oxidation states of Tb.

The element distribution profile in the multilayer stack, obtained through XPS spectroscopy and integrated spectra of O, Fe, Co, and Tb on both pre- and post-annealed samples, is depicted in Figure 5a). The oscillations observed in the profile align with the multilayer nanostructured composition of the material, where the diminishing amplitude is a result of averaging induced by abrasion. Notably, the oscillations of Tb and Fe are out of phase, as anticipated with alternating FeCo and TbCo2 layers. However, the Co oscillations are in phase with Fe oscillations and not with Tb oscillations which seems contradictory with the stoichiometry of the considered alloys, the $TbCo_2$ layer being enriched in Co compared to FeCo. This inconsistency suggests an inhomogeneous element distribution in the alloys. In annealed samples, oscillation period decreases down the stack, indicating layer refinement during annealing. Moreover, increased O composition after annealing in the first $TbCo_2$ layers suggests internal migration of O towards the surface, possibly driven by a concentration gradient, akin to outgassing in a vacuum environment.

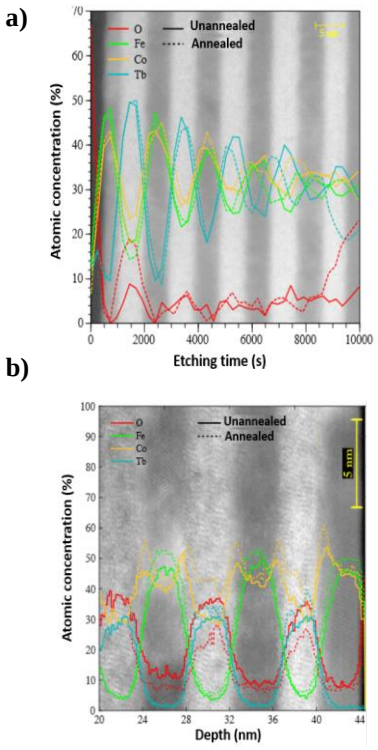

Figure 5 : a) Comparison of the distribution profiles of the elements O, Fe, Co and Tb in the complete FeCo/$TbCo_2$ stack obtained by integration of the XPS spectra produced during the abrasion of the annealed and post-annealed stack. b) Comparison of the distribution profiles of the elements O, Fe, Co and Tb at the bottom of the FeCo/$TbCo_2$ stack obtained by EDS analysis before and after annealing at 300 °C.

XPS spectroscopy provides insights into the atomic composition of the stack and the impact of thermal annealing. To validate these insights, micro-analysis using EDS coupled with TEM imaging was conducted, capitalizing on the lateral spatial resolution of atomic element distribution. Figure 5b) displays the atomic distribution profile of O, Fe, Co, and Tb in the lower section of the stack before and after annealing, alongside the TEM image. Remarkably, element distribution exhibits heterogeneity in both alloys. The atomic compositions of oxygen (O), iron (Fe), cobalt (Co), and terbium (Tb) were determined through EDS mapping, as depicted in Figure 6. In the unannealed sample, the FeCo alloy core aligns closely with the expected composition ($Fe_{48}Co_{42}O_{10}$ versus $Fe_{50}Co_{50}$). Conversely, the $TbCo_2$ alloy core exhibits stoichiometry close to $Tb_{32}Co_{32}O_{36}$ compared to $Tb_{33}Co_{67}$, indicating Co depletion in the core layer due to Co enrichment at interfaces, particularly pronounced at the FeCo/$TbCo_2$ interface. This enrichment results from Co diffusion into the FeCo phase during $TbCo_2$ deposition, continuing until the formation of the first Tb monolayer, which acts as a barrier. The Co enrichment in the FeCo phase and depletion in the $TbCo_2$ phase is less pronounced at the FeCo/$TbCo_2$ interface, where Tb is already present during FeCo deposition. Profiles of O, Fe, Co, and Tb element distributions in the multilayer stack were derived by integrating EDS mapping, representing X-ray impacts per second discriminated by energy, providing an account of atomic element distribution. Figure 6 illustrates an assembly based on these mappings for annealed and post-annealed samples.

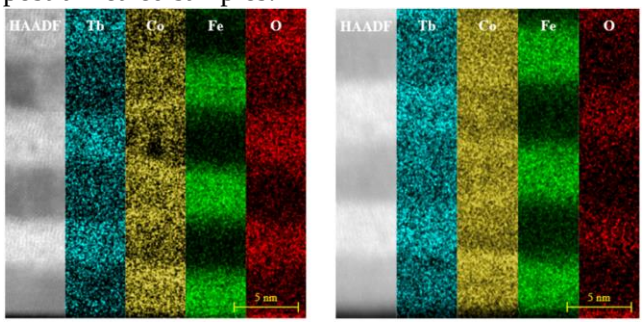

a) b)

Figure 6 : Assembly of the EDS maps of the atomic distribution of the elements Tb, Co, Fe and O compared with the TEM image is shown for the unannealed sample a) and the annealed one at 300°C b).

The atomic composition of the elements O, Fe, Co and Tb at the core of the layers and at the $TbCo_2$/FeCo and FeCo/$TbCo_2$ interfaces before and after annealing are shown in Tables 1 and 2.

% at.	Tb	Co	Fe	O
TbCo	29.5 33.6	29.6 40.6	4.6 5.0	36.3 20.8
FeCo	2.0 2.2	42.0 42.2	4.5 49.6	9.5 6.0

Table 1 : Atomic composition of the elements Tb, Co, Fe and O in the core of the $TbCo_2$ and FeCo layers for the ante (blue) and post-annealed at 300 °C (red) samples.

% at.	Tb	Co	Fe	O
TbCo / FeCo	15.3 17.9	42.3 47.0	20.6 22.0	21.8 13.1
FeCo / TbCo	12.0 15.3	44.5 48.4	28.1 27.2	15.4 9.1

Table 2 : Atomic composition of the elements Tb, Co, Fe and O at the $TbCo_2$/FeCo and FeCo/$TbCo_2$ for the annealed (blue) and post-annealed at 300 °C (red) samples.

Observation of the EDS maps reveals the effect of thermal annealing on the atomic distribution of the elements at the core of the FeCo/$TbCo_2$ multilayer stack. It is clear that Co and Tb are redistributed within

the stack during annealing. More specifically, the core of the $TbCo_2$ phase is enriched in Co, its atomic concentration rising from 30% to 40%. This enrichment occurs at the expense of O, which falls from 36% to just 20%. The atomic concentration of Tb remains virtually stable, rising from 29% to 33%. The atomic distribution of the elements in the core of the FeCo phase remains virtually identical after annealing, with only a depletion in O (atomic concentration divided by two) to the benefit of Fe. Regarding the interfaces, post annealing Co enrichment and O depletion can be observed. Thanks to XPS spectroscopy analysis performed on the same samples as described in Figure 4, the various compounds present in each of the layers of the stack, in particular the metal oxides naturally present alongside the TbCo and FeCo alloys, could be estimated. It shows the presence of Co(II) and Fe(III) in the FeCo layer, potentially compatible with the formation of the cobalt ferrite $CoFe_2O_4$, as well as Tb (III) and (IV) oxides in almost identical proportions in the TbCo layer. From all these observations, we can write the following equilibria:

Before annealing :

$$Tb_{32}Co_{32}O_{36} = 10.6\ TbCo_3 + 6.6\ Tb_2O_3 + 8\ TbO_2 \quad (2)$$

After annealing :

$$Tb_{36}Co_{43}O_{21} = 23.5\ TbCo_{1.8} + 3.9\ Tb_2O_3 + 4.6\ TbO_2 \quad (3)$$

TEM imaging also provides information on the crystal structure of the alloys within the $FeCo/TbCo_2$ multilayer stack. Figure 7 shows the crystallographic structure of the stack before and after annealing at 300 °C. In both cases, the FeCo phase is polycrystalline with a grain size of a few nanometers, while the $TbCo_2$ phase is completely amorphous. However, on a larger scale numerous quasi-epitaxial zones are found in FeCo after annealing, which may contribute to some extent to the improvement in the magnetostriction coefficient. In addition, the interfaces appear to be better defined after annealing, certainly due to the atomic rearrangement.

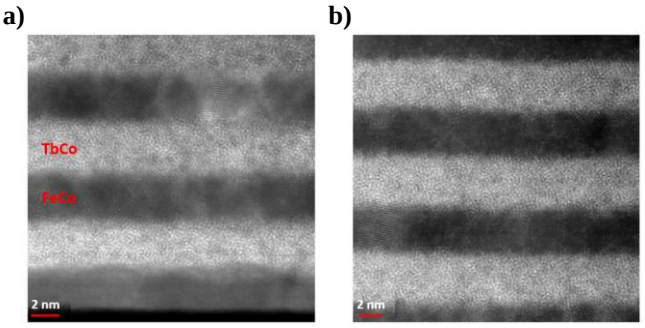

Figure 7 : HAADF images of the $FeCo/TbCo_2$ multilayer stack, a) unannealed and b) annealed at 300°C in a vacuum and magnetic field, highlighting the polycrystalline nature of the FeCo phase and the amorphous nature of the TbCo phase.

From these observations, we can conclude that the strong enrichment of Co at the interfaces, particularly emphasized after thermal annealing, is partly responsible for the decrease in the anisotropy field due to lower exchange energy with Tb compared to Fe. In addition, the redistribution of Co after annealing promotes the formation of the TbCo alloy at the expense of terbium oxides, in a stoichiometry close to the (1:2) ratio, enhancing the magnetostriction coefficient $b^{\gamma,2}$until it reaches its maximum value of -7.3 MPa at 300°C, starting from a deposited magnetic film with a base magnetostriction of about -5.2 MPa. Ultimately, the overall depletion of oxygen arises from a vacuum annealing effect, wherein the remaining oxygen bonds with metallic terbium (Tb) and iron (Fe) elements. This process further disrupts the interaction between the rare earth (Tb) and transition metal (Fe or Co) elements. Regarding the microstructure, the FeCo phase is polycrystalline, even right after deposition, while the $TbCo_2$ remains amorphous even after thermal annealing.

5. Equivalent piezomagnetic model

The authors previously developed an equivalent piezomagnetic model to explore magnetoelastic coupling in piezo-electro-magnetic composites the applied model is based on the assumption of effective magnetic properties and magnetic domain effects are neglected. For more details, refer to [19-20]. The piezomagnetic equations stem from studying a magnetoelastic wave in a ferromagnetic thin film on a piezoelectric substrate. This involves linearizing coupled mechanical and magnetic equations, Newton's motion equation and the Landau-Lifshitz equation around the magnetization's ground state position. The bias magnetic field's direction and magnitude determine the position of the ground state magnetization. The piezomagnetic equations are given by :

$$\rho \frac{\partial^2 u_i}{\partial t^2} = \frac{\partial \sigma_{ij}}{\partial x_j}, \quad (4)$$

$$\frac{\partial b_i}{\partial x_i} = \frac{\partial \left(\mu_0 (h_i + m_i)\right)}{\partial x_i}. \quad (5)$$

In this context, ρ stands for the density of the ferromagnetic thin film, u_i represents the particle displacement components within the film, m_i dynamic aimantation, h_i magneto static field, and x_i refers to the

Eulerian coordinates (following Einstein's summation convention where i, j, k, and l span from 1 to 3, aligning with the x, y, z axes). The model provides the dynamic stress tensor components, denoted as σ_{ij}, and the dynamic magnetic induction components, represented by b_i.

$$\sigma_{ij} = \left(C_{ijkl} + \Delta C_{ijkl}\right)\frac{\partial u_k}{\partial x_l} - q_{ij}h_l, \quad (6)$$

$$b_i = q_{ijkl}\frac{\partial u_k}{\partial x_l} + u_{il}h_l. \quad (7)$$

The equivalent piezomagnetic constitutive equations include the elastic stiffness constants C_{ijkl}, adjustments to the effective magnetic permeability μ_{ij}, and corrections to the elastic stiffness constants ΔC_{ijkl} .

$$\mu_{il} = \mu_0(\delta_{il} + \chi_{il}), \quad (8)$$

$$\Delta C_{ijkl} = b_{ijmn}(M_n^0 q_{mkl} + M_m^0 q_{nkl}). \quad (9)$$

The constants b_{ijmn} represent the magnetoelastic constants. Specifically, the magnetostriction is assumed isotropic, with b_{1111} corresponding to $b^{\gamma,2}$ in Callen's notation [21]. The piezomagnetic constants q_{ijk} and the magnetic susceptibility expressions χ_{il} are detailed in [20]. Additionally, both q_{ijk} and χ_{il}, as shown in formula (9), rely on the static magnetization M^0 of the magnetostrictive film and there on the applied external magnetic field. These factors influence ΔC_{ijkl}. To consider the intricacies of magnetization in thin magnetic films, the model relies on the relationship between the external magnetic field applied and the resulting static magnetization, derived from measured magnetization characteristics, see Figure 2. The velocity of surface acoustic waves within the multilayer system, comprising a magnetostrictive thin film, a piezoelectric substrate, and an SiO_2 layer, is determined using the effective piezomagnetic material model described. This is done in tandem with the numerical Legendre/Laguerre polynomial expansion method outlined comprehensively in [20]. The phase shift ($\Delta\varphi$) of the S_{21} parameter is correlated with the variation in velocity (Δv) of the specific SAW mode under consideration by:

$$\left|\frac{\Delta\varphi}{\varphi_0}\right| = \frac{L_{film}}{L} * \left|\frac{\Delta v}{v_0}\right|, \quad (10)$$

Here, Δv represents the difference between $v(H)$ and v_0, where v_0 is the velocity of the SAW without a magnetic field, and $v(H)$ is the velocity under a specific applied magnetic field H. Additionally, $\Delta\varphi$ signifies the difference between $\varphi(H)$ and φ_0. Here, $\varphi(H)$ represents the phase of the S_{21} parameter under a given applied magnetic field H, and φ_0 is defined as $2\pi f\frac{L}{v_0}$, where L denotes the propagation length and f denotes the frequency used. L_{film} magnetic film length along the propagation path

6. Experimental Results vs Theoretical Model

The S_{21} phase shift measurement was conducted to observe how it varies with the applied magnetic field for both shear horizontal and Rayleigh waves before and after thermal annealing of the functionalized SAW device at different temperatures.

Figure 8 illustrates the electro-acoustic SAW response (S_{21} parameter) to the applied external magnetic field of both acoustic SH and Rayleigh waves for a propagation path of 2 mm. It shows an increase of the sensitivity with the annealing temperature, confirming equation (1), which shows the FOM material enhancement for lower anisotropy (Figure 2a)) and higher magnetostriction coefficient (Figure 3). Figure 8 also highlights the remarkable agreement between theoretical model predictions and experimental results. It should be noted that the resonance frequency of the SAW sensor varies by a few kHz with increasing temperature, but the measurements are always conducted at the resonance frequency of the sensor.

a)

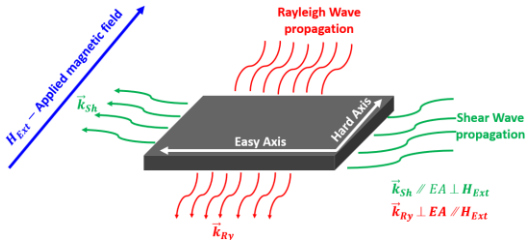

b)

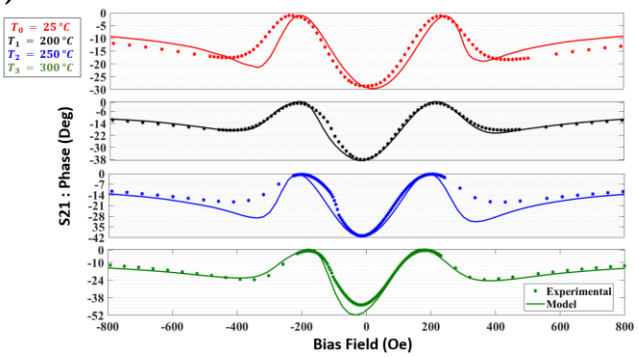

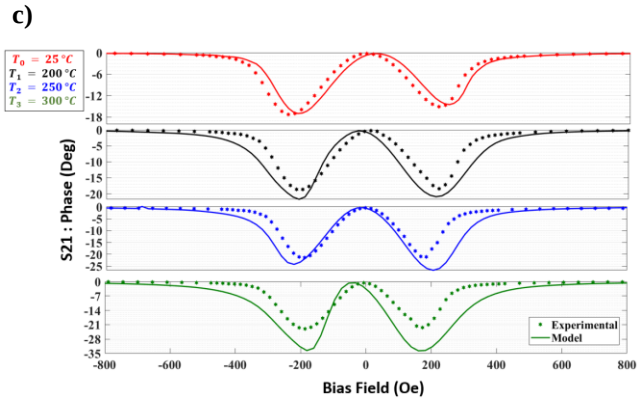

Figure 8 : a) The S_{21} phase response is shown as a function of the bias magnetic field applied along the hard axis of the thin film at different annealing temperature, red without annealing, black annealing at 200 °C, blue annealing at 250 °C and green annealing at 300 °C : b) SH wave, c) Rayleigh wave.

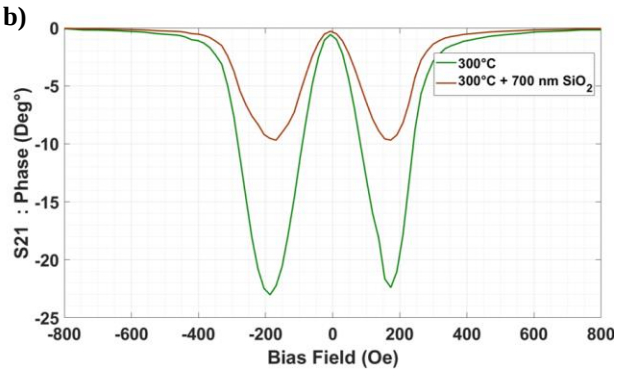

Figure 9 : Sensitivity variation of the SAW sensor annealed at 300 °C (Green curve), in terms of phase shift as a function of the applied magnetic field , is observed with the deposited SiO_2 thin film (Brown curve): a) Increased sensitivity for the SH wave. b) Decreased sensitivity for the Rayleigh acoustic wave.

Figure 9 shows the impact of coating only the surface of the nanostructured FeCo/$TbCo_2$ thin film with a layer of SiO_2 [22-23] with a thickness of 700 nm, see Figure 10, that will act as an effective protective shield, protecting the film from potential deterioration caused by the environmental conditions surrounding the sensor, As described in the theoretical studies conducted in reference [10]. The study indicates a 2.5-fold increase in the difference between the maximum and minimum phase shift for the SH acoustic wave. This improvement is attributed to the addition of SiO_2 on top of the multilayer thin film which convert the SH wave into a guided Love wave. This modification enhances the confinement of the mode close to the sensitive layer, which explains the improved sensitivity. Unlike the SH wave, the Rayleigh wave loses sensitivity as it does not rise to the surface, but penetrates more deeply into the piezoelectric quartz substrate, leading to a reduction in sensitivity by a factor of 2.5.

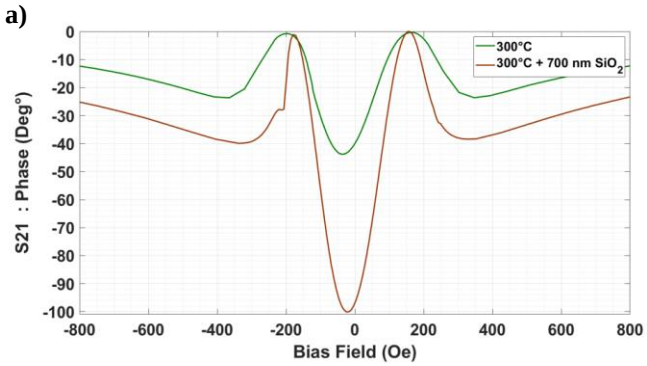

Based on the experimental findings and the piezomagnetic model described earlier, the theoretical evolution of the sensitivity of shear horizontal and Rayleigh waves regarding the thickness of the SiO_2 guiding layer deposited atop the nanostructured thin film was examined. Figure 10 reports the obtained results and shows that the sensitivity of SH wave increases with the SiO_2 guiding layer thickness, reaching its maximum sensitivity for 700 nm. In contrast, the sensitivity of the Rayleigh wave decreases with the increase of the SiO_2 guiding layer thickness, reaching its minimum for the same thickness, 700 nm.

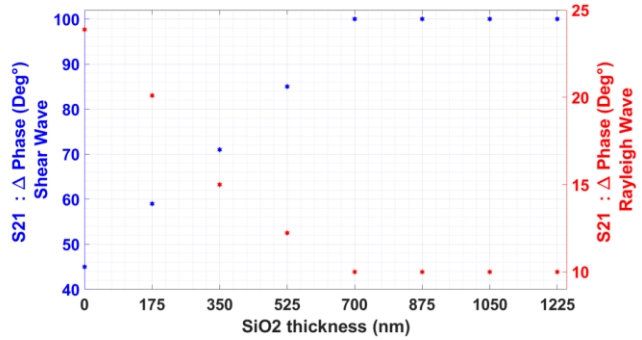

Figure 10 : Sensitivity evolution of SH wave (blue curve) and Rayleigh wave (red curve) versus the thicknesses of the SiO_2 guiding layer deposited on top of the nanostructured multilayer magnetic thin film.

7. Conclusion

In conclusion, we investigated the influence of thermal annealing under vacuum and bias magnetic field on the magnetic properties of nanostructured multilayered

$FeCo/TbCo_2$ thin film. The study showed that increasing the annealing temperature reduces the anisotropy field H_A and increases the magnetostriction coefficient $b^{\gamma,2}$, which leads to an overall rise of the FOM of the magnetic thin film. This behavior is mainly attributed to the evolution of the atomic distribution within the nanolayers relative to the annealing temperature. Increasing the FOM of the magnetic thin film improved the sensitivity to the magnetic field of the SH and Rayleigh wave-based SAW sensors. The effect of capping the magnetostrictive thin film with a SiO_2 guiding layer on the sensitivity to the magnetic field was also investigated. It was shown that the sensitivity of SH waves was improved thanks to the guiding layer turning them into Love wave, contrary to the Rayleigh wave that penetrates deeper into the quartz substrate. The experimental results concerning the sensitivity to magnetic fields of the fabricated magnetoelastic SAW devices were accurately elucidated by the developed equivalent piezomagnetic model.

Acknowledgement

We acknowledge support from the French National Research Agency (ANR) in the framework of ANR 20-CE42-0009 project. It is also supported by the CPER EE4.0 project and the company JEUMONT Electric. The authors also thank RENATECH, the French national nanofabrication network.

References

[1] H. Greve et al., “Giant magnetoelectric coefficients in (Fe90 Co10)78 Si12 B10 -AlN thin film composites,” Appl. Phys. Lett., vol. 96, no. 18, May 2010, Art. no. 182501, doi: 10.1063/1.3377908.

[2] N. Tiercelin et al., “Magnetoelectric effect near spin reorientation tran- sition in giant magnetostrictive-aluminum nitride thin film structure,” Appl. Phys. Lett., vol. 93, no. 16, Oct. 2008, Art. no. 162902, doi: 10.1063/1.3001601.

[3] M. Bichurin et al.,“Magnetoelectric current sensors,” Sensors, vol. 17, no. 6, p. 1271, Jun. 2017, doi: 10.3390/s17061271.

[4] S. Zabel et al., “Phase modulated magnetoelectric delta-E effect sensor for sub-nano tesla magnetic fields,” Appl. Phys. Lett., vol. 107, no. 15, Oct. 2015, Art. no. 152402, doi: 10.1063/1.4932575.

[5] A. Kittmann et al., “Wide band low noise love wave magnetic fieldsensor system,” Sci. Rep., vol. 8, no. 1, p. 278, Jan. 2018, doi:10.1038/s41598-017-18441-4.

[6] M. Kadota et al.,“Magnetic sensor based on surface acoustic wave resonators,” Jpn. J. Appl. Phys., vol. 50, no. 7, Jul. 2011, Art. no. 07HD07.

[7] H. Mishra et al.,“Temperature compensated magnetic field sensor based on love waves,” Smart Mater. Struct., vol. 29, no. 4, Mar. 2020, Art. no. 045036, doi: 10.1088/1361-665X/ab7857.

[8] A. Mazzamurro et al., “Giant magnetoelastic coupling in a love acoustic waveguide based on TbCo2/FeCo nanostructured film on ST-cut quartz,” Phys. Rev. A, Gen. Phys., vol. 13, no. 4, Apr.2020,Art.no.044001,doi:10.1103/PhysRevApplied.13.044001.

[9] H. Zhou et al., “Multilayer magnetostrictive structure based surface acoustic wave devices,” Appl.Phys. Lett., vol. 104, no. 11, Mar. 2014, Art. no. 114101, doi:10.1063/1.4868530.

[10] O. Marbouh et al., "Enhancing magnetoelastic coupling in shear surface acoustic waveguide based on ST-Cut Quartz substrate and Ni thin films with uniaxial magnetic anisotropy induced by thermal annealing," in IEEE Sensors Letters, doi: 10.1109/LSENS.2023.3330639.

[11] E. Quandt et al., “Magnetic properties and microstructure of giant magnetostrictive TbFe/FeCo multilayers,” Journal of Applied Physics, vol. 83, no. 11, pp. 7267–7269, 1998.

[12] E. Quandt et al., “Giant magnetostrictive spring magnet type multilayers,” Journal of Applied Physics, vol. 81, no. 8, pp. 5420– 5422, 1997.

[13] N. Duc et al., “Large magnetostrictive susceptibility in Tb–FeCo/FeCo multilayers,” Applied Physics Letters, vol. 78, no. 23, pp. 3648–3650, 2001.

[14] E. Lacheisserie et al., “Magnetostriction and internal stresses in thin films: the cantilever method revisited,” Journal of Magnetism and Magnetic Materials, Volume 136, Issues 1–2, 1994, Pages 189-196, ISSN 0304-8853.

[15] N. Tiercelin, “ Phénomènes dynamiques non linéaires dans les films minces magnétostrictifs au voisinage de la Transition de Réorientation de Spin. Application aux micro systèmes,” These, France, 2000.

[16] D.D. Sarma et al., “XPES studies of oxides of second- and third-row transition metals including rare earths,” Journal of Electron Spectroscopy and Related Phenomena, vol. 20, pp. 25–45, 1980

[17] B. D. Padalia et al., “X-Ray Photoelectron Core-Level Studies of the Heavy Rare-Earth Metals and Their Oxides,” Proc R Soc London Ser A, vol. 354, no. 1678, pp. 269–290, 1977.

[18] M. Glätzle et al., “The high-pressure oxide tb3o5 and its non-centrosymmetric low temperature polymorph-a comprehensive study,” Chemistry, vol. 24, 10 2018.

[19] O. Bou Matar et al., “Legendre and Laguerre polynomial approach for modeling of wave propagation in layerd magneto-electro-elastic media”, J. Acoust. Soc. Am. 133, 1415 (2013).

[20] O. Bou Matar et al., “Band gap tunability of magneto-elastic phononic crystal”, Journal of Applied Physics 111, 54901 (2012).

[21] E. R. Callenand et al., “Static Magnetoelastic Coupling in Cubic Crystals”, Physical Review 129, 578 (1963).

[22] Y. Yang et al., "Enhanced Performance Love Wave Magnetic Field Sensors With Temperature Compensation," in *IEEE Sensors Journal*, vol. 20, no. 19, pp. 11292-11301, 1 Oct.1, 2020, doi: 10.1109/JSEN.2020.2998826.

[23] H. Mishra et al., "Microstructured Multilayered Surface-Acoustic-Wave Device for Multifunctional Sensing",Phys. Rev. Applied 14, 014053,https://doi.org/10.1103/PhysRevApplied.14.014053.